

Traversing Double-Well Potential Energy Surfaces: Photoinduced Concurrent Intralayer and Interlayer Structural Transitions in XTe_2 ($\text{X} = \text{Mo}, \text{W}$)

Yingpeng Qi,^{*,#} Mengxue Guan,[#] Daniela Zahn, Thomas Vasileiadis, Hélène Seiler, Yoav William Windsor, Hui Zhao, Sheng Meng,^{*} and Ralph Ernstorfer^{*}



Cite This: *ACS Nano* 2022, 16, 11124–11135



Read Online

ACCESS |



Metrics & More



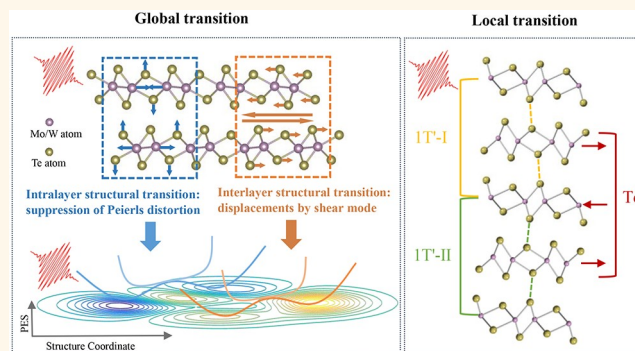
Article Recommendations



Supporting Information

ABSTRACT: The microscopic arrangement of atoms and molecules is the determining factor in how materials behave and perform; *i.e.*, the structure determines the property, a traditional paradigm in materials science. Photoexcitation-driven manipulation of the crystal structure and associated electronic properties in quantum materials provides opportunities for the exploration of exotic physics and practical applications; however, a generalized mechanism for such symmetry engineering is absent. Here, by ultrafast electron diffraction, structure factor calculation, and TDDFT-MD simulations, we report the photoinduced concurrent intralayer and interlayer structural transitions in the Td and 1T' phases of XTe_2 ($\text{X} = \text{Mo}, \text{W}$). We discuss the modification of multiple quantum electronic states associated with the intralayer and interlayer structural transitions, such as the topological band inversion and the higher-order topological state. The twin structures and the stacking faults in XTe_2 are also identified by ultrafast structural responses. The comprehensive study of the ultrafast structural response in XTe_2 suggests the traversal of all double-well potential energy surfaces (DW PES) by laser excitation, which is expected to be an intrinsic mechanism in the field of photoexcitation-driven global/local symmetry engineering and also a critical ingredient inducing the exotic properties in the non-equilibrium state in a large number of material systems.

KEYWORDS: photoinduced structural transition, topological transition, double-well potential energy surfaces, ultrafast electron diffraction, stacking faults, global/local symmetry engineering



INTRODUCTION

Within the transition metal dichalcogenides (TMDCs) family, MoTe_2 and WTe_2 (*i.e.*, XTe_2 ($\text{X} = \text{Mo}, \text{W}$)) have recently sparked broad research interest for their rich structural phases and unusual electronic structures, such as the semiconductor-to-semimetal structural transition,^{1,2} the extremely large magnetoresistance,^{2,3} the quantum spin Hall effect,^{4–7} and the topological phases.^{8–14} At room temperature, MoTe_2 is in its 1T' phase and forms a layered structure with double sheets of Te atoms bound together by interleaving Mo atoms, as shown in Figure 1A. By lowering the temperature to below 250 K, bulk MoTe_2 undergoes a structural transition from the monoclinic 1T' to the orthorhombic Td phase. These two semimetallic phases hold distinct interlayer stackings while exhibiting the same intralayer crystal structure with a Peierls

distortion.² The intralayer Peierls distortion is characterized by the Mo–Mo metallic bonds, as shown in Figure 1A. Such exotic Mo–Mo metallic bonds modulate the adjacent Mo atoms by alternating shorter and longer distances and also drive the out-of-plane wrinkling of the Te atoms. The 1T' phase of MoTe_2 belongs to the centrosymmetric space group $P2_1/m$, and the Td phase belongs to the non-centrosymmetric space group $Pmn2_1$. As the sister compound of MoTe_2 , WTe_2

Received: April 19, 2022

Accepted: July 1, 2022

Published: July 6, 2022



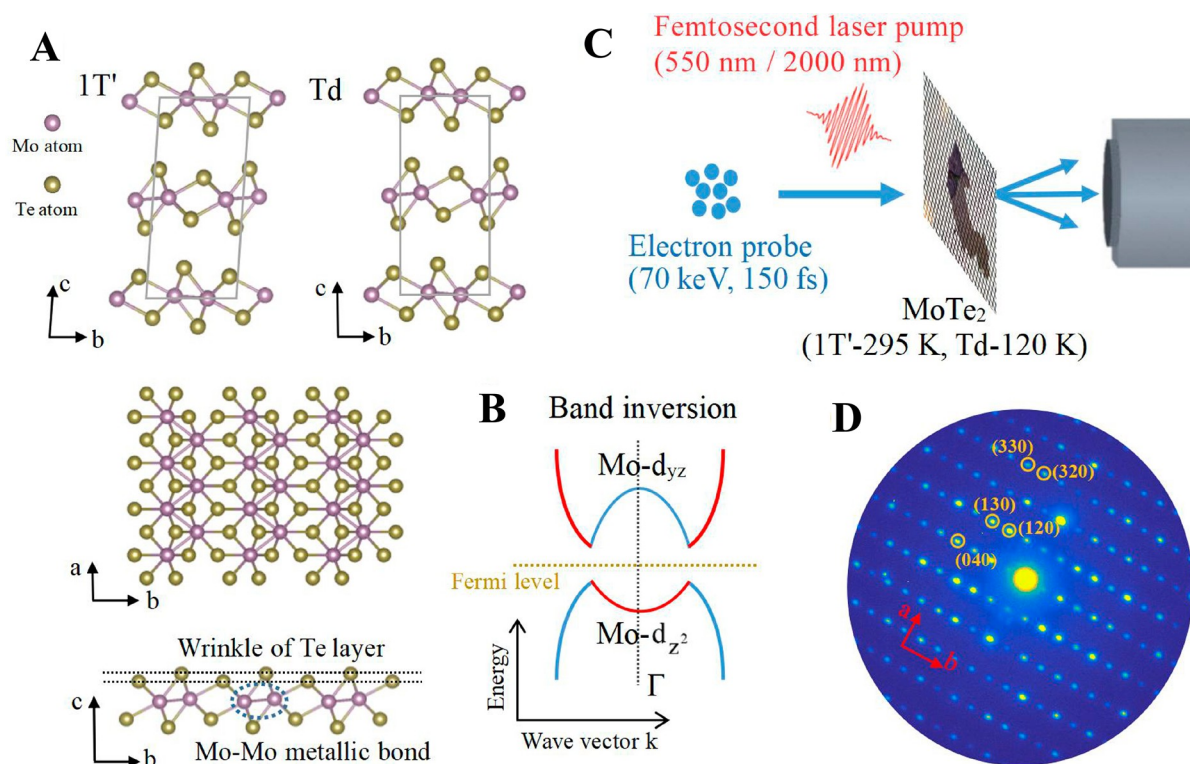


Figure 1. Crystal structure of MoTe₂ and the diffraction pattern obtained in femtosecond electron diffraction experiment. (A) The unit cell of MoTe₂ in the monoclinic 1T' phase and the orthorhombic Td phase. The bottom shows the top view (*a*-*b* plane) and the side view (*b*-*c* plane) of the crystal structure of a single layer. The two phases hold the same in-plane crystal structure but different vertical stacking. (B) Schematic band inversion by intralayer Peierls distortion in monolayer 1T' MoTe₂. (C) Schematic presentation of the ultrafast electron diffraction experiment. The femtosecond laser pumps the MoTe₂ nanofilm with the crystal phase controlled by the temperature. Another femtosecond electron pulse diffracts off the crystal, thus probing transient structural changes. (D) A prototypical diffraction pattern of MoTe₂ in the experiment. Several spots are labeled by circles.

has commonly been observed in the Td phase at the room temperature and below. Both the 1T' and Td phases of XTe₂ are topologically non-trivial. In particular, the bulk Td phase is a type-II Weyl semimetal;^{8–12,15} meanwhile, the bulk Td phase and the 1T' phase are also a higher-order topological insulator.^{13,14,16} The crystalline topological phase of electrons is intrinsically protected by the symmetry of the crystal.^{17–21} Therefore, triggering an intralayer or interlayer symmetry change offers prospects in practical applications such as topological switch electronics. Except for topological materials, that structure determines property is the traditional paradigm in the field of materials science.

Regarding the interlayer symmetry in XTe₂, an interlayer stacking transition with the THz field pump as well as the 2100 nm laser pump is observed in the Td phase of WTe₂.²² Consequently, the Weyl semimetal phase is switched to the trivial phase with the flattening of the interlayer double-well potential energy surface (DWPEs) by coherent interlayer shear displacement. With infrared (800 nm) and mid-infrared (2600 nm) laser pumps,²³ a similar topological switch in the Td phase of MoTe₂ is observed through ultrafast spectroscopy, suggesting a laser field driven interlayer transition. The recent angle-resolved photoemission spectroscopy (ARPES) study with 827 nm laser excitation shows that the interlayer shear mode can be described by a π -shifted sine function, implying an impulsive excitation of this shear mode and proving the model of field-driven stacking transition.²⁴ Therefore, with infrared and mid-infrared laser excitation, the interlayer transition is pervasively attributed to the laser field,^{22–24} akin

to the model with the THz pump.²² However, in this field driven stacking transition model, the electron–phonon interaction induced by the above-band-gap photon excitation is neglected. A direct observation of the ultrafast interlayer stacking transition with a structural probe is required to identify the transition mechanism.

In XTe₂, the intralayer Peierls distortion brings about the onset of many physical phenomena, such as anisotropic optical and electronic properties.²⁵ More importantly, the intralayer distortion induces the band inversion. Such a band inversion causes the monolayer XTe₂ to become a topological insulator^{2,4,5,17} and the bulk to become a higher-order topological insulator.^{13,14,16} A schematic illustration of the band inversion in monolayer 1T' MoTe₂ is shown in Figure 1B. With the inclusion of spin–orbit coupling (SOC), the band hybridization and the lifting of degeneracies at the Dirac cones (driven by the band inversion) open a bandgap in bulk and monolayer XTe₂.^{2,4,5} The topological band inversion and the bandgap opening are the hallmarks of a quantum spin Hall state in monolayer 1T' XTe₂.^{4–7} Therefore, a dynamic control of the intralayer Peierls distortion will modulate such exotic quantum electronic properties in XTe₂.

Here we report a comprehensive study of the ultrafast structural response in the 1T' and the Td phases of XTe₂ (X = Mo, W) with 550 and 2000 nm laser excitation. By ultrafast electron diffraction (UED), structure factor calculation and time-dependent density functional theory molecular dynamics (TDDFT-MD) simulations, we identify concurrent interlayer and intralayer structural transitions, indicated by the interlayer

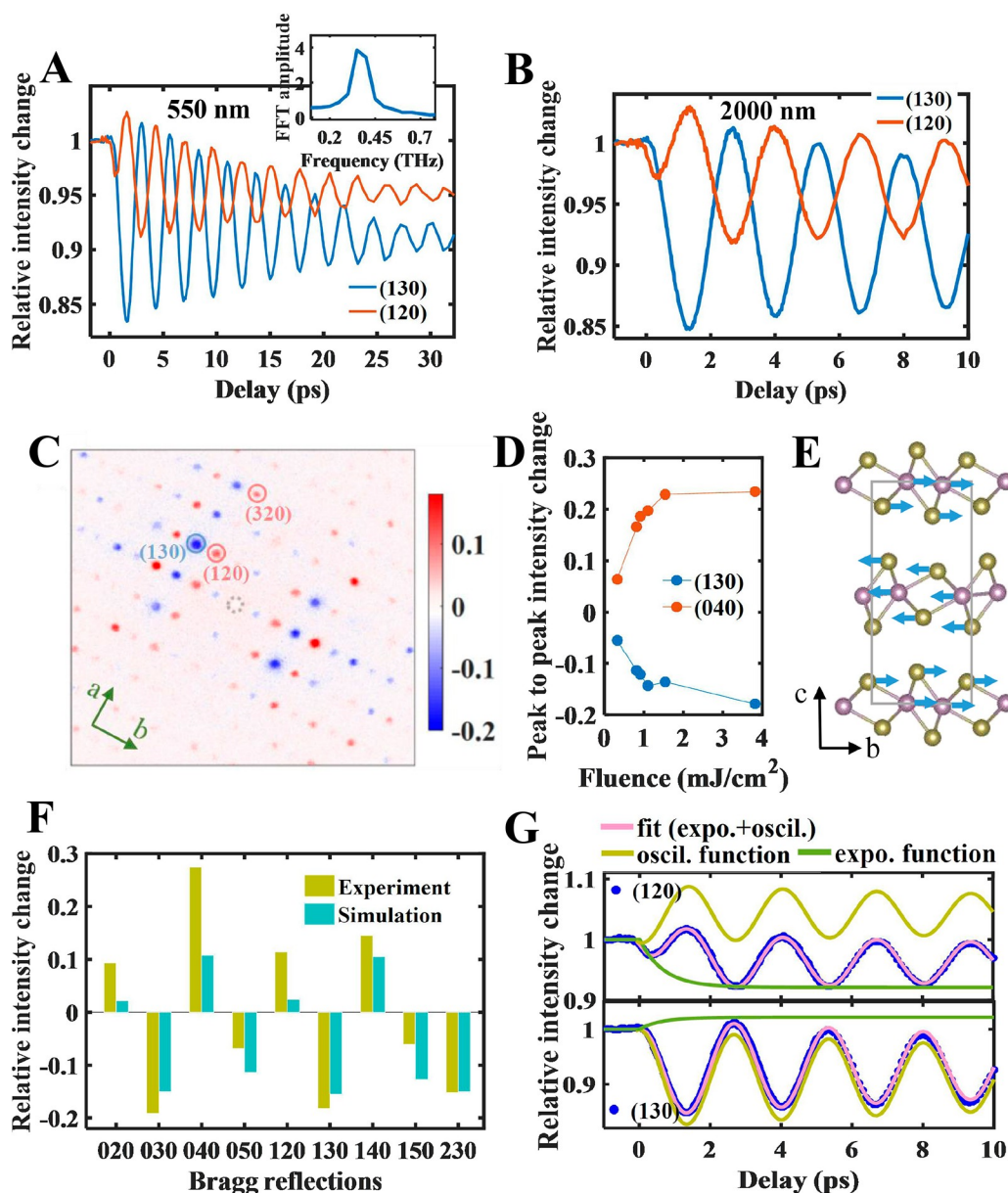


Figure 2. Photoinduced interlayer shear mode in the Td phase of MoTe₂. (A, B) Intensity changes with 550 nm (3.81 mJ/cm²) and 2000 nm (15.08 mJ/cm²) laser pump. The fast Fourier transformation (FFT) amplitude of oscillations in the inset indicates the ~ 0.4 THz shear phonon mode. (C) Difference map of the intensity between the delay points of 1.6 and 2.9 ps with 550 nm (3.81 mJ/cm²) laser pump. (D) Peak-to-peak intensity change of the intensity oscillation of the (130) and (040) reflections as a function of the pump fluence. (E) Schematic illustration of the interlayer shear mode. (F) Bar chart showing the shear mode induced intensity changes of several peaks in the experiment (550 nm and 3.81 mJ/cm²) and the simulation. The shear displacement of each layer is 0.015 Å. (G) The fit of the intensity oscillation of the (120) and (130) reflections. The pink solid curve is the best fit, which is composed of an exponential function (the green curve) and an exponentially decaying cosine function (the yellow curve). The pump laser is 2000 nm and 15.08 mJ/cm².

shear displacement and the reduction of the intralayer Peierls distortion, respectively. The interlayer shear mode is well described by a π -shifted cosine function indicating a dispersive excitation of this coherent phonon mode. Therefore, the interlayer structural transition is driven by the electron–phonon coupling, distinct from the model of laser field driven transition.^{22–24} An ultrafast Mo–Mo (W–W) bond stretching within 0.3 ps is revealed in both the 1T' and the Td phases, triggering an ultrafast suppression of the intralayer Peierls distortion. We discuss the modification of multiple quantum electronic states associated with the intralayer and interlayer structural transitions. The twin structures and the stacking

faults in the 1T' and the Td phases of XTe₂ are also identified by the ultrafast structural response. By far, a benchmark of the ultrafast structural responses and the symmetry engineering by photoexcitation in quantum materials and materials with complex crystalline structures is not clear. Based on the comprehensive study of XTe₂, we propose the traversal of all double-well potential energy surfaces (DWPES) driven by ultrafast photoexcitation, which is expected to be an intrinsic mechanism in the field of global/local symmetry engineering and also a critical ingredient inducing exotic properties in the non-equilibrium state in a large number of material systems.

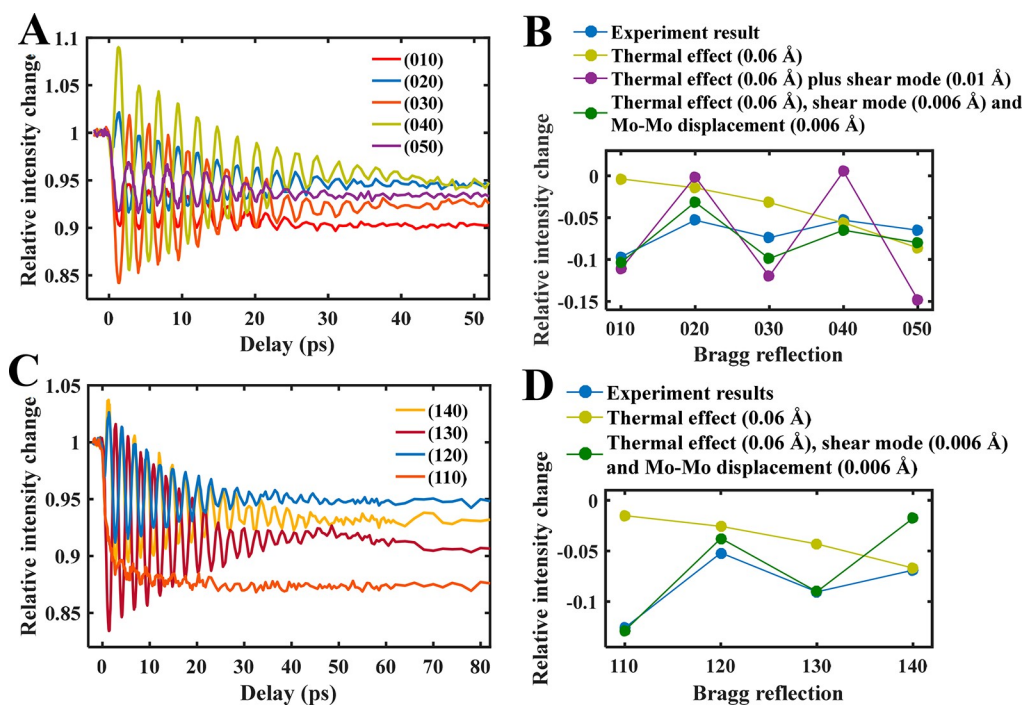


Figure 3. Photoinduced interlayer shear displacement and intralayer Mo–Mo displacement in the Td phase of MoTe₂. The pump laser is 550 nm and 3.81 mJ/cm². (A) Long-term evolution of the intensity of the (0k0) reflections. (B) Experimental intensity change of the (0k0) reflection at the time delay of 50 ps and the structure factor calculation of the intensity change. The thermal effect, the interlayer shear displacement, and the intralayer Mo–Mo bond stretching are involved in the calculation. (C) Long-term evolution of the intensity of the (1k0) reflections. (D) Experimental intensity change of the (1k0) reflection at the time delay of 80 ps and the structure factor calculation of the intensity change.

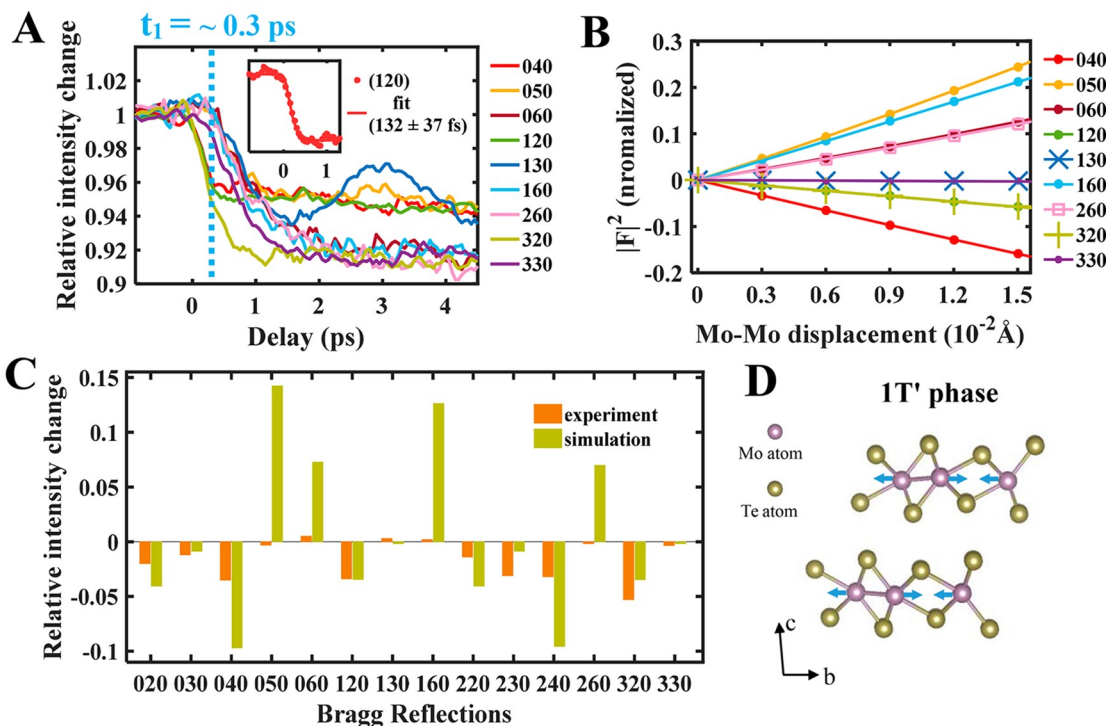
RESULTS AND DISCUSSION

Ultrafast Electron Diffraction and Diffraction Pattern of XTe₂. The MoTe₂ and WTe₂ film used in the experiment are prepared by mechanical exfoliation from a bulk crystal (HQ graphene). The thickness of the freestanding film on the TEM grid is >30 nm, characterized by the propagation of the breathing phonon mode induced by laser excitation.²⁶ A schematic representation of the ultrafast electron diffraction experiment is depicted in Figure 1C. Visible (550 nm) and mid-infrared (2000 nm) femtosecond laser pulses are employed to electronically excite the nanofilm of MoTe₂ (and WTe₂). We choose these two pump wavelengths in order to revisit the mechanism of the interlayer transition, where a field driven transition model is pervasive in previous studies.^{22–24} After laser excitation, another femtosecond electron pulse subsequently probes the structural changes at a varying time delay. The temporal resolution of the system is estimated to be ~150 fs (fwhm).²⁷ The crystalline phase of the ground state MoTe₂ in the experiment is controlled by the temperature, *i.e.*, the 1T' phase at room temperature of 295 K and the Td phase at 120 K. The WTe₂ holds the same phase, *i.e.*, the Td phase, at room temperature and low temperature. A prototypical experimental diffraction pattern of the MoTe₂ in the Td phase is shown in Figure 1D.

Interlayer Structural Transition by Shear Displacement. To investigate the transient structural dynamics, we focus on the relative intensity change of the Bragg reflections as a function of time delay. For the Td phase of MoTe₂, pronounced intensity oscillation of the Bragg reflection is observed with both 550 and 2000 nm laser excitation, as shown in Figure 2A,B. The frequency of the oscillation is ~0.4 THz. Such a low frequency oscillation with a lifetime of ~40 ps

is attributed to the interlayer shear phonon mode;^{23,28} *i.e.*, the atoms in the same layer vibrate along the same direction while atoms in two adjacent layers vibrate toward opposite directions. The oppositely phased intensity oscillations along the *b* axis (*i.e.*, (h20), (h30), (h40), (h50)) are shown in Figure 2C and Figure S1, indicating that the intensity oscillations arise from the interlayer shear phonon.²² A similar shear mode oscillation in the sister compound WTe₂ is observed and shown in Figure S2. In Figure 2D, with improving the pump fluence, the amplitude of the shear mode increases linearly then saturates somewhat at the higher fluence (the threshold fluence before damage is 5.44 mJ/cm² with 550 nm laser pump). A schematic illustration of the interlayer shear displacement is displayed in Figure 2E. Such an interlayer shear mode has been identified as a signature of an electronic transition from the Weyl semimetal to the trivial phase.^{22,23} We calculate the shear displacement induced intensity changes by structure factor calculation (see the details of the calculation in Materials and Methods). In the calculation, to modulate the shear displacement relative to the equilibrium position, the adjacent layers move in opposite direction along the *b* axis by 0.015 Å and then –0.015 Å. The calculated intensity change qualitatively agrees with the experimental result as shown in Figure 2F. Except the Td phase, the emergence of unexpected shear mode is observed in the 1T' phase (see Figure S3). Together with the disappearance of the intensity oscillation for Bragg reflections belonging to the same family of lattice plane (see Figure S4), we attribute these unexpected structural dynamics to the twin structures and the interlayer stacking faults (see details in section 2 of the Supporting Information).

1T' phase (295 K)



Td phase (120 K)

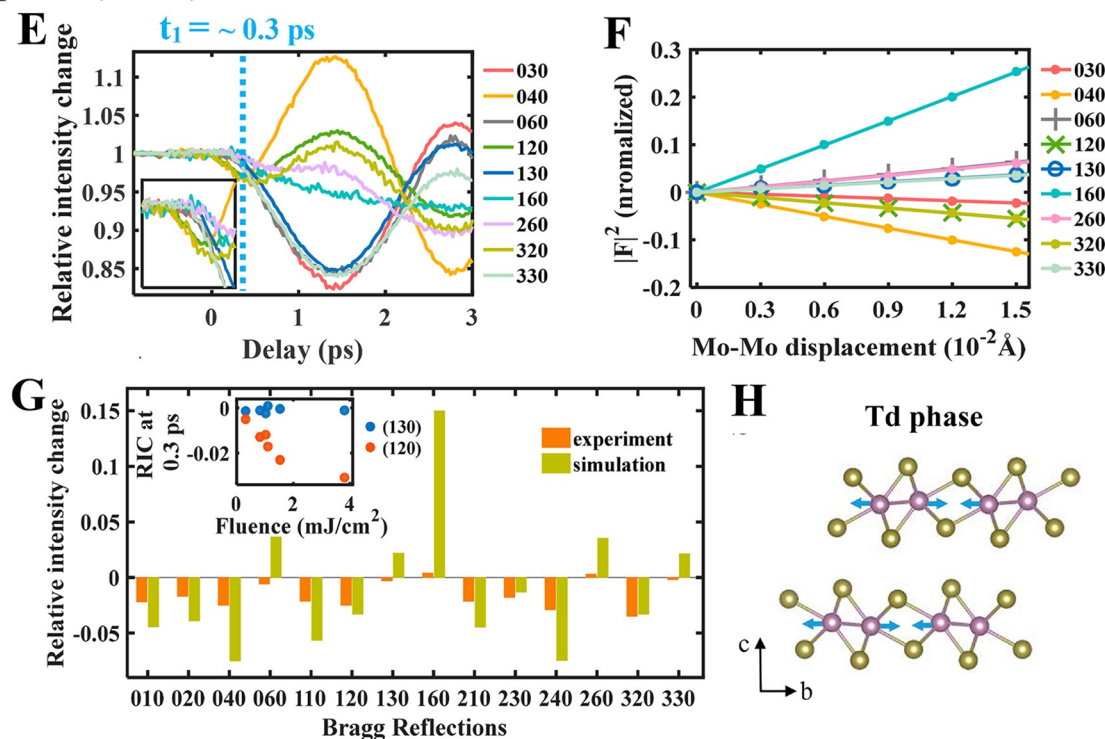


Figure 4. Photoinduced intralayer structure transition by Mo–Mo bond stretching in the 1T' (A–D) and Td (E–H) phases of MoTe₂. (A) Anisotropic intensity changes (a prompt decay vs a delayed decay) of Bragg reflections in the 1T' phase within ~ 0.3 ps with 2000 nm (13.10 mJ/cm²) laser excitation. The inset is the fit of the intensity decay of the (120) reflection. (B) Structure factor calculation of the intensity changes as a function of Mo–Mo displacement (bond stretching). (C) Bar chart showing the calculated intensity changes vs the experimental changes. The Mo–Mo displacement is 0.006 Å (bond stretching of 0.012 Å). (D) Schematic illustration of the Mo–Mo bond stretching in the 1T' phase. (E) Anisotropic intensity change of Bragg reflections in the Td phase within ~ 0.3 ps with 2000 nm (15.08 mJ/cm²) laser excitation. The inset zooms in on the intensity change within sub-ps. (F) Structure factor calculation of the intensity changes as a function of Mo–Mo displacement. (G) Bar chart showing the calculated intensity changes vs the experimental changes. The Mo–Mo displacement is 0.006 Å. The inset is, with 550 nm laser excitation, the fluence dependence of the relative intensity changes (RIC) of (120) and (130) reflections at the time delay of 0.3 ps. (H) Schematic illustration of the Mo–Mo bond stretching in the Td phase.

In Figure 2G, the shear phonon mode is fitted by a combination of an exponential function and an exponentially decaying cosine function, *i.e.*, $A \exp(-t/\tau_1) + B \cos(2\pi ft + \varphi) \exp(-t/\tau_2)$. The frequency f and the phase φ of the best fit are 0.38 ± 0.001 THz and -0.15 ± 0.01 rad, respectively. More fitting and discussion about the fit function are shown in Figure S5. The identified cosine fitting of the shear mode indicates a displacive excitation of this coherent phonon mode (DECP).^{29,30} In this case, the ultrafast electronic excitation gives rise to the immediate change of the potential energy surface (PES)^{29–31} and the symmetry changes toward a higher symmetry phase. The time scale of the symmetry change by DECP would be within one-quarter of the oscillation period.^{32,33} In the case of XTe_2 , the established equilibrium position corresponding to the shear mode is achieved within half the period, as shown in Figure 2. The one-quarter of the oscillation period (~ 0.66 ps) is in good agreement with that of the topological switch through ultrafast spectroscopy (~ 0.6 ps in ref 23.), evidencing the DECP nature of the topological switch. We do not observe a two-step shear displacement as that in previous study.³⁴

With the intensity change at the equilibrium state (≥ 50 ps), we evaluate the interlayer structure transition induced by the shear displacement and other contributions to the intensity change. Figure 3A displays the long-term evolution of the intensity of the (0*k*0) reflections in the Td phase of MoTe_2 with 550 nm laser excitation. Generally, the thermal effect, *i.e.*, the Debye–Waller effect, induces a progressively larger intensity change for higher scattering vector peaks. Therefore, the much larger intensity decrease of the (010) reflection than that of other (0*k*0) reflections suggests the structural response beyond a thermal effect. We model the intensity changes by structure factor calculation (see the details of the calculation in Materials and Methods). The intensity change of (*h*00) reflections is used to quantify the thermal effect after laser excitation (see Figure S6). The corresponding atomic displacement by thermal effect is identified to be ~ 0.06 Å. In Figure 3B, introducing the shear displacement gives rise to a larger intensity decrease of the (010) reflection. However, the intensity change of the (020), (040), and (050) reflections still deviates away from the experimental results significantly. Modulating the amplitude of the shear displacement is not working. Note that, besides the interlayer shear displacement, we have identified the intralayer Mo–Mo bond stretching (*i.e.*, the suppression of the Peierls distortion) in the next section, which should be added to the structural response model at the equilibrium state. As shown in Figure 3B, the combination of the Debye–Waller (0.06 Å), the shear displacement (0.006 Å), and the Mo–Mo bond stretching (0.006 Å) gives rise to a good agreement between the calculated intensity change and the experimental results (see details on the fit in section 5 of the Supporting Information). Based on this model, a good agreement between the calculation and the experiment result for the (1*k*0) reflection is shown in Figure 3C,D. The same experimental structure response with 2000 nm laser excitation is also observed in the Td phase of MoTe_2 and WTe_2 (see Figure S7). Therefore, we identify both the interlayer and intralayer structural transitions at the equilibrium state (≥ 50 ps).

Intralayer Structural Transition by the Suppression of the Peierls Distortion. To gain further insight into the ultrafast structural response except the shear mode, we focus on the intensity change of Bragg reflections on femtosecond

time scale. For the 1T' phase, the time-dependent intensity change is shown in Figure 4A with 2000 nm laser excitation. Within $t_1 = 0.3$ ps, anisotropic intensity changes for Bragg reflections are observed; for example, the intensity of the (040), (120), and (320) reflections decays significantly, while the intensity of the (060), (130), and (330) reflections stays unchanged. The time constant for the intensity decay of (120) is 132 ± 37 fs fitted by an exponential function, as shown in the inset in Figure 4A, which is much faster than the equilibrium of the overall lattice system (see Figure S6). The same anisotropic intensity change is observed in the Td phase of MoTe_2 (as shown in Figure 4E) and WTe_2 (see Figure S2). Since both the 1T' and Td phases exhibit the same intralayer Peierls distortion, we speculate a possible structural transition associated with the suppression of the intralayer Peierls distortion.² The anisotropic intensity change within 0.3 ps is against the trend of the intensity modulation by the shear displacement as displayed in Figure 4E; therefore, the dominating structural response is not the interlayer transition in this time scale.

For XTe_2 , the Fermi surface nesting drives the intralayer Peierls distortion² characterized by the in-plane Mo–Mo metallic bonds and the out-of-plane wrinkling of Te and Mo atoms, as shown in Figure 1A. Generally, the femtosecond laser excitation induces the flattening of the double-well potential energy surface and subsequently suppresses the structural distortion, giving rise to a higher crystal symmetry in many material systems.^{32,33,35–38} In the case of MoTe_2 , the femtosecond laser induces a population in the antibonding d-orbitals of Mo atoms,^{39,40} then the shorter Mo–Mo distance (*i.e.*, the Mo–Mo metallic bonds) could get elongated. By structure factor calculation, we calculate the intensity change of Bragg reflections by introducing a Mo–Mo bond stretching in the unit cell of the 1T' phase and the Td phase. The possible reduction of the out-of-plane wrinkling along the *c* axis is neglected in the calculation, since the experiment is not sensitive to such out-of-plane motions. Figure 4B and F display the calculated intensity change as a function of the Mo–Mo bond stretching in the 1T' phase and the Td phase of MoTe_2 (see the details of the calculation in Materials and Methods). The similar anisotropic intensity changes for Bragg reflections as that of experimental results in Figure 4A,E are observed in the calculation results. The bar charts in Figure 4C,G display the qualitative agreement between the calculation and the experimental results. The discrepancy between the quantified intensity change of the experiment and the calculation results may derive from the neglected Debye–Waller factor of Mo and Te, the concurrent shear displacement, and the identified interlayer stacking faults in the sample. By structure factor calculation of the element-dependent Debye–Waller effect (see Figure S9), we conclude that the Debye–Waller effect plays a minor role in the structural response within 0.3 ps. Therefore, together with the structural response at the equilibrium state (≥ 50 ps) in Figure 3, we attribute the ultrafast anisotropic intensity changes to the intralayer structure transition, *i.e.*, the Mo–Mo (W–W) bond stretching, in XTe_2 . The A_g mode with a frequency of 112 cm^{-1} could be the phonon mode dominating the intralayer structure transition.⁴¹ With 2000 nm laser excitation, the same anisotropic intensity change as that with 550 nm laser excitation is observed (see Figure S8).

Photoinduced Intralayer and Interlayer Atomic Motions from TDDFT-MD Simulation. To further confirm

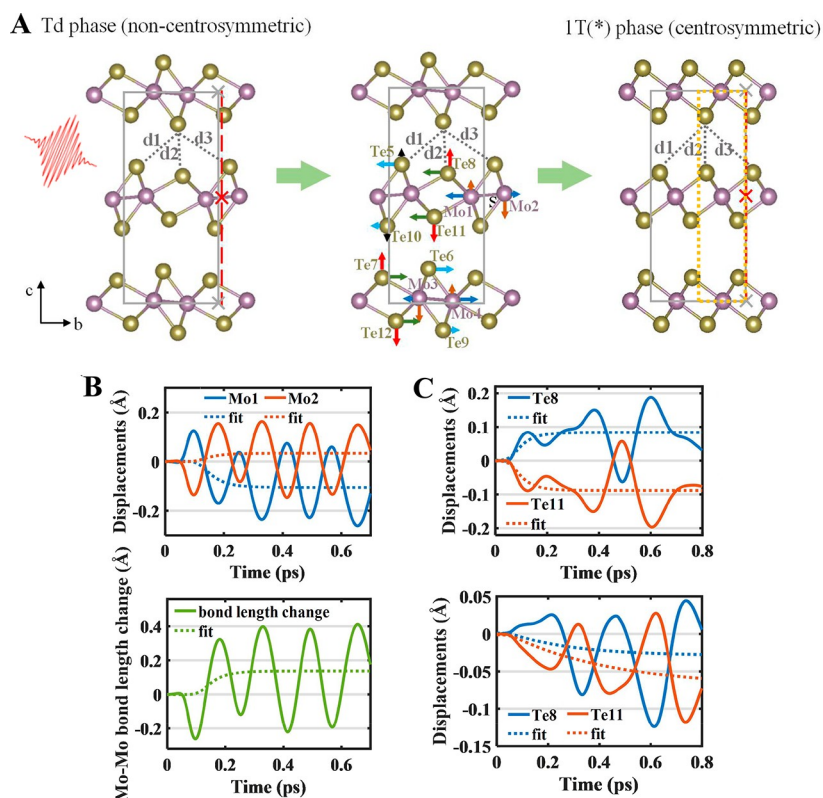


Figure 5. Photoinduced intralayer and interlayer structural transition in the Td phase of MoTe_2 by TDDFT-MD simulations. (A) In-plane and out-of-plane movements of Mo and Te atoms indicated by arrows. The gray rectangle is the unit cell of the Td phase. The gray crosses are symmetry centers of top and bottom layers, and the red cross is the symmetry center of the middle layer. An intermediate state 1T(*) with an intralayer structure akin to the undistorted 1T phase is formed. The bond length $d_3 > d_1$ in the Td phase, while $d_3 = d_1$ in the 1T(*) phase. The dotted yellow rectangle is the unit cell of the 1T(*) phase. (B) Top: Time-dependent displacements of Mo1 and Mo2 along the b axis. Bottom: Time-dependent Mo–Mo bond length change between Mo1 and Mo2. The dotted curves are the monoexponential fit of the simulation results. (C) The time-dependent displacements of Te8 and Te11 along the c axis (top) and the b axis (bottom). The dotted curves are the monoexponential fits of the simulation results.

the concurrent intralayer and interlayer atomic motions, we perform TDDFT-MD simulations for MoTe_2 in its Td phase. The pump fluence is set to 2 mJ/cm^2 close to the experimental condition. More detailed information regarding the simulation can be found in **Materials and Methods**. Figure 5 shows the simulation results. The arrows in Figure 5A indicate the averaged directional movements of Mo and Te atoms in the unit cell. Detailed displacement trajectories with time for atoms in the middle layer (the bottom layer) are summarized in Figure 5B,C (Figure S10B–S10D). As shown in Figure 5B (bottom), the bond length of Mo1 and Mo2 stretches significantly within $\sim 0.3 \text{ ps}$, which agrees with the ultrafast bond stretching from the experimental results. Meanwhile, Te8 and Te11 move in opposite directions along the c axis as displayed in Figure 5C (top), which reduces the out-of-plane wrinkling. The stretching of the metallic bonds and the reduction of the out-of-plane wrinkling within 0.3 ps evidence the photoinduced suppression of the intralayer Peierls distortion. Note that Te8 and Te11 also move simultaneously along the negative direction of the b axis, as shown in Figure 5C (bottom), while Te7 and Te12 in the adjacent layer move along the positive direction of the b axis (see Figure S10C (bottom)). Such an opposite movement along the b axis between two adjacent layers is a signature of the interlayer shear displacement. The intensity change of several Bragg reflections is calculated based on the atomic displacements at 0.2 ps in Figure 5. The calculated anisotropic intensity change,

as shown in Figure S11, agrees qualitatively with the experimental results in Figure 4. The simulation results in Figure 5 contains some coherent oscillations of the atomic displacements with a period of $200\text{--}300 \text{ fs}$, which are not observed in experimental results. Such coherent oscillations could be attributed to the excitation of high-frequency ($\sim 4 \text{ THz}$) phonon modes.^{24,42} The $\sim 150 \text{ fs}$ temporal resolution of our experimental system is insufficient to detect such ultrafast oscillation.

Overall, the simulation results in Figure 5 unambiguously demonstrate the concurrent interlayer shear displacement and the suppression of the intralayer Peierls distortion, in agreement with the experimental results. A schematic illustration of such a structural change is summarized in Figure 5A. On the sub-ps time scale, the intralayer Peierls distortion is suppressed giving rise to a 1T-like structure. Meanwhile, the shear displacement reduces the bond length discrepancy between d_1 and d_3 , and the interlayer stacking is changed correspondingly, as shown in Figure 5A. When the symmetry center of the top (and bottom) layer (*i.e.*, the gray crosses) gets aligned to that of the center layer (*i.e.*, the red cross), a structural transition from the non-centrosymmetric to the centrosymmetric can be achieved by the shear displacement. We define an intermediate centrosymmetric 1T(*) phase with the 1T-like intralayer structure (Figure 5A (right)). Therefore, the photoexcitation induces a structural transformation from the non-centrosymmetric Td phase (Figure 5A

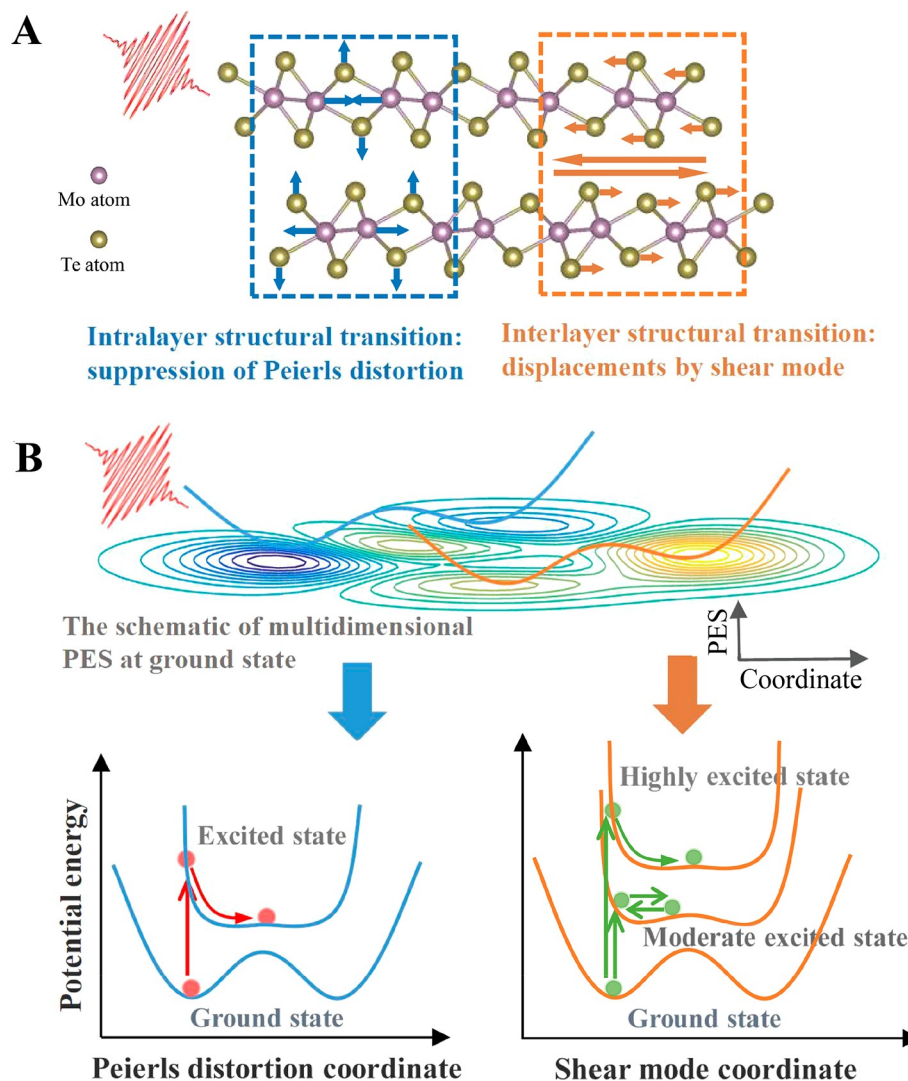


Figure 6. Schematic presentation of the concurrent intralayer and interlayer structural transitions in real space and the corresponding changes of the double-well potential energy surfaces in the Td phase of XTe_2 . (A) Photoinduced intralayer structural transition by the suppression of the Peierls distortion and interlayer structural transition by the shear displacement. The main atomic motions in the intralayer transition include the dissociation of Mo–Mo bonds and the reduction of the out-of-plane wrinkling of Te atoms. (B) Top: Schematic illustration of the multidimensional potential energy surfaces at the ground state in the Td phase of XTe_2 . Bottom: Schematic of the modulation of the potential energy surfaces of the Peierls distortion and the shear mode by photoexcitation. The flattened potential energy surface gives rise to the suppression of Peierls transition to a 1T-like intralayer structure. For the potential energy surface of the shear mode, at a low excitation density, a coherent shear phonon mode is excited. At a high excitation density, the symmetry switches from the non-centrosymmetric to the centrosymmetric in a sub-period of the shear phonon mode.

(left)) to the centrosymmetric 1T(*) phase (Figure 5A (right)). Note that the unit cell of the 1T(*) phase, indicated by the dotted rectangular in Figure 5A (right), will be half of the unit cell of the Td phase (the gray rectangle) along the b axis, which may be a signature for further experimental study on such a structural transition. In our experiment, the inhomogeneous longitudinal excitation due to the limited optical penetration depth and the identified interlayer stacking faults (see Figures S3 and S4) may blur the underlying unit cell change.

CONCLUSIONS

In this work, with femtosecond electron diffraction, structure factor calculations, and TDDFT-MD simulations, we reveal the photoexcitation induced concurrent intralayer and interlayer structural transitions in the 1T' and the Td phases of XTe_2 (X

= Mo, W). The pathway of the concurrent structural transitions in the real space and the sketch of the corresponding PES modulation by photoexcitation in the Td phase of MoTe_2 are illustrated in Figure 6A and B, respectively. For the intralayer structural transition, the photoexcitation induces the occupation of the antibonding d-orbitals of Mo atoms, inducing the stretching of the in-plane metallic Mo–Mo bonds. The Mo–Mo bonds stretching and the reduction of the out-of-plane wrinkling of Te atoms give rise to an ultrafast suppression of the Peierls distortion and a transition to intralayer 1T-like structure within 0.3 ps. Accompanied with the intralayer transition, the photoinduced interlayer shear displacement produces a transition, *i.e.*, the interlayer structural transition, to a centrosymmetric phase within one-quarter of the period of the shear phonon mode. From the perspective of potential energy surfaces, the photoexcitation flattens the

DWPES along the Peierls distortion coordinate and the shear mode coordinate, as shown in Figure 6B (bottom), giving rise to the concurrent structure transitions. A simple question is that if there is any correlation between the intralayer and the interlayer structural transition, for example, will the intralayer structural transition facilitate or impede the interlayer shear transition, which needs to be studied further. In contrast to the complete interlayer transition on the surface layer of bulk MoTe_2 by ultrafast spectroscopy,^{22,23} the displacement corresponding to both the interlayer and intralayer transition is ~ 0.01 Å in our UED experiment, much smaller than the required displacement for a complete transition (0.19 and 0.43 Å, respectively). The discrepancy may derive from the limited optical penetration depth and the identified interlayer stacking faults. In addition, the electron–phonon thermalization (or the Debye–Waller effect) may be another significant energy relaxation pathway,⁴³ competing with the structural transitions. The twin structures and the stacking faults in both the $1\text{T}'$ and the Td phases of XTe_2 are identified by the ultrafast structural response (see Figures S3 and S4), which indicates the suppression of the local DWPES corresponding to defects in XTe_2 . Therefore, ultrafast electron diffraction is expected to be a powerful tool to reveal twin structures and stacking faults in a large number of material systems.

The revealed ultrafast structural responses in our work update perspectives for the control of associated electronic properties in XTe_2 ($\text{X} = \text{Mo}, \text{W}$). First, we clearly identify the displacive excitation of the interlayer shear mode. Therefore, the electron–phonon coupling is demonstrated to be the driving force of the transition from the photoinduced Weyl semimetal phase to the trivial phase, which is distinct from the model of THz/light field driven transition in refs 22–24. Second, the intralayer Peierls distortion causes the band inversion.^{2,14,17} Consequently, the topological insulator phase in monolayer^{2,4,5,17} and the higher-order topological insulator phase in the bulk $1\text{T}'$ and Td phase^{13,14,16} are expected to switch to the trivial phase upon suppression of the intralayer Peierls distortion. Moreover, the quantum spin Hall state based on the topological band inversion in the monolayer $1\text{T}'$ phase of XTe_2 ^{4–7} will also be modulated by the intralayer transition; Third, the recent study suggests an ultrafast Lifshitz transition within 0.4 ps in the Td phase of MoTe_2 .⁴⁴ Due to the absence of precise knowledge on the structural response in this time scale, such an electronic transition is attributed to the dynamic modification of the Coulomb interaction.⁴⁴ The ultrafast suppression of the intralayer Peierls distortion within 0.3 ps, revealed in our work, will modify the Fermi surface and therefore contribute to the ultrafast Lifshitz transition. Further study is required to identify the detailed correlation between the structural transition and the electronic transition.

The photoexcitation-driven modification of the potential energy surface and the associated structural transition present the opportunity for manipulating the properties of materials and have been widely explored in material systems.^{32,33,35–38} However, in all these studies, the structural transition mainly contains single DWPES, which is also termed as the Mexican-hat potential energy surface and the potential energy surface with saddle point, or focuses on the order parameter of a simple potential energy surface. In our results of XTe_2 ($\text{X} = \text{Mo}, \text{W}$), the concurrent interlayer and intralayer structural transitions indicate the traversal of the two DWPES by photoexcitation, which is beyond the previous concept on single DWPES based structural transition. Consequently, the

traversal of all DWPES achievable by the photon-generated carriers is conceivable in complex material systems with multidimensional potential energy surfaces (*i.e.*, multidimensional structural distortions). Except for the above global structure transition, photoinduced ultrafast transition of the local structure associated with local DWPES, such as the local stacking faults in this work and the local correlated structure in ref 45 (see more information about local correlated structures in ref 46), is also confirmed. Therefore, the traversal of all DWPES is expected to be an intrinsic mechanism dominating the photoexcitation-driven global/local symmetry engineering and structural transitions. The traversal of all DWPES, either global or local, in material system can be used to guide the property control by photoexcitation and also to identify the multidimensional local energy minimum. For example, the controversial atomic structure in β phase of $2\text{D III}_2\text{–VI}_3$ materials,⁴⁷ *i.e.*, the Mexican-hat PES for the middle layer atoms, could be identified by photoinduced ultrafast structural response. We also speculate that the traversal of DWPES could be expanded to study and identify the local structure and local symmetry in amorphous materials and glasses.^{48,49} Ultrafast electron/X-ray diffraction is a powerful tool leading the research along this way.

The recent study suggests the disorder (or multimode)-driven ultrafast structural transition and the order parameter on a simple potential energy surface play minor roles.^{36,50} In our work, the concept of the traversal of all DWPES in a photoexcitation-driven structural transition, involving coherent and incoherent evolution of multiphonon modes, may be a clearer transition regime than the disorder-driven transition model.^{36,50} Except for the phonons, electronic excitation by ultrafast laser would also intertwine with other degrees of freedom, such as the electron and the spin; however, in most cases,^{44,51,52} the DWPES associated with structural distortions is neglected in building the transition model. Since the belief that structure determines property is the traditional paradigm in the field of materials science, the traversal of DWPES and the associated structural transition suggest determining the ultrafast structural response before attributing the photoinduced exotic property change to the perturbation of other degrees of freedom in material systems.

MATERIALS AND METHODS

Ultrafast Electron Diffraction Experiment. In the ultrafast electron diffraction experiment, a 70-keV DC electron diffraction setup is used to study the ultrafast atomic motion during the photoinduced phase transitions. The electron pulses were set to a few thousand electrons per pulse with a spot size of ~ 100 μm diameter at the sample position. The transverse spot size of the pump laser is ~ 400 μm , which is much larger than the spot size of the electron pulse to keep a relative homogeneous excitation of the detected area on the sample. The repetition rate of the pump laser is 1 kHz, and the pump wavelength is tuned by commercial TOPAS facility. The instrument response function duration of the UED system is estimated to be ~ 150 fs fwhm.²⁷ The base temperature of the sample is controlled by liquid nitrogen. The thickness of the freestanding film on the TEM grid is characterized by the propagation of the breathing phonon mode induced by laser excitation. Though a weak breathing mode is measured suggesting the thickness of ~ 30 nm, the exfoliated film is not that homogeneous indicating the overall thickness of the film could be larger than 30 nm. The structural dynamics measurements in the text also suggest the thickness of the film >30 nm.

Structure Factor Calculation for the Interlayer and Intralayer Structure Transitions and the Debye–Waller Effect. The

intensity of a Bragg peak, $I \propto |F|^2$, can be calculated using the structure factor:

$$F(hkl) = \sum_j f_j \exp[-i2\pi(hx_j + ky_j + lz_j)] \quad (1)$$

where the summation runs over all atoms in the unit cell (four Mo and eight Te atoms), f_j is the atomic scattering factor for the j th atom, $r_j = x_j\hat{a} + y_j\hat{b} + z_j\hat{c}$ is the vector position of the atom in the unit cell, and (hkl) are the Miller indices. For the Debye–Waller effect, we introduce the atomic Debye–Waller factor into the structure factor calculation:

$$T_j = \exp(-M), \quad M = 8\pi^2\mu^2(\sin\theta/\lambda)^2 \quad (2)$$

M denotes the Debye–Waller factor and μ^2 represents the mean square displacement of Mo or Te atom.

To simulate the interlayer and intralayer structure transition, we calculate the intensity modulation $\Delta I/I_0$ by introducing the interlayer shear displacement and the Mo–Mo bond stretching. For the interlayer shear displacement of the trilayer construction in the unit cell, we define the atoms in the top and bottom layer displacement as Δy , while the atoms in the medium layer are displaced $-\Delta y$. The structure factor in this case is

$$F(hkl, \Delta y) = \sum_{\text{top and bottom}} f_j T_j \exp[-i2\pi(hx_j + k(y_j + \Delta y) + lz_j)] + \sum_{\text{medium}} f_j T_j \exp[-i2\pi(hx_j + k(y_j - \Delta y) + lz_j)] \quad (3)$$

For the intralayer Mo–Mo bond stretching, the displacement of Mo atoms is introduced into the above equation in a similar way as that of the shear displacement. The structure factor calculated by the algebra equation has been compared with that from SingleCrystal to confirm reliable structure factor calculation in this work.

Methods for TDDFT-MD Simulations. The experimental geometry of the bulk MoTe_2 is adopted, which is characterized by an orthorhombic (Td) unit cell without inversion symmetry.⁵³ To study the optoelectronic responses of MoTe_2 in Td phase, linearly polarized laser beams with time-dependent electric field $E(t) = E_0 \cos(\omega t) \exp[-(t - t_0)^2/2\sigma^2]$ are applied along the crystallographic a -axis. The photon energy, width, and amplitude are set as 2.25 eV ($\lambda = 550$ nm), 15 fs, and 0.06 V/Å, respectively. This setup allows us to reproduce a laser fluence (ca. 2 mJ/cm²) similar to experimental measurements.

The TDDFT-MD calculations are performed using the time-dependent *ab initio* package (TDAP) as implemented in SIESTA.^{54–56} The bulk MoTe_2 in its Td phase is simulated with a unit cell of 12 atoms with periodical boundary conditions. Numerical atomic orbitals with double- ζ polarization (DZP) are employed as the basis set. The electron–nuclear interactions are described by Troullier–Martins pseudopotentials, PBE functional.⁵⁷ An auxiliary real-space grid equivalent to a plane-wave cutoff of 250 Ry is adopted. To make a good balance between the calculation precision and cost, a Γ -centered $6 \times 5 \times 3$ k -point grid is used to sample the Brillouin zone. The coupling between atomic and electronic motions is governed by the Ehrenfest approximation.⁵⁸ During dynamic simulations the evolving time step is set to 0.05 fs for both electrons and ions in a microcanonical ensemble.

ASSOCIATED CONTENT

Supporting Information

The Supporting Information is available free of charge at <https://pubs.acs.org/doi/10.1021/acsnano.2c03809>.

Further details on the structural response with 550 and 2000 nm laser excitation, the fitting of the interlayer shear mode, the quantification of the displacements of the interlayer and intralayer displacement, the Debye–Waller effect at the equilibrium state, the identification

of the twin structures and stacking faults, and the TDDFT-MD simulation results (PDF)

AUTHOR INFORMATION

Corresponding Authors

Yingpeng Qi – Fritz-Haber-Institut, Max-Planck-Gesellschaft, Berlin 14195, Germany; Center for Ultrafast Science and Technology, School of Physics and Astronomy, Shanghai Jiao Tong University, Shanghai 200240, China; orcid.org/0000-0001-5950-8157; Email: qiyp@sjtu.edu.cn

Sheng Meng – Beijing National Laboratory for Condensed Matter Physics and Institute of Physics, Chinese Academy of Sciences, Beijing 100190, P. R. China; School of Physical Sciences, University of Chinese Academy of Sciences, Beijing 100049, China; orcid.org/0000-0002-1553-1432; Email: smeng@iphy.ac.cn

Ralph Ernstorfer – Fritz-Haber-Institut, Max-Planck-Gesellschaft, Berlin 14195, Germany; orcid.org/0000-0001-6665-3520; Email: ernstorfer@fhi-berlin.mpg.de

Authors

Mengxue Guan – Beijing National Laboratory for Condensed Matter Physics and Institute of Physics, Chinese Academy of Sciences, Beijing 100190, P. R. China

Daniela Zahn – Fritz-Haber-Institut, Max-Planck-Gesellschaft, Berlin 14195, Germany; orcid.org/0000-0002-7606-0961

Thomas Vasileiadis – Fritz-Haber-Institut, Max-Planck-Gesellschaft, Berlin 14195, Germany; orcid.org/0000-0001-7720-8801

Hélène Seiler – Fritz-Haber-Institut, Max-Planck-Gesellschaft, Berlin 14195, Germany; orcid.org/0000-0003-1521-4418

Yoav William Windsor – Fritz-Haber-Institut, Max-Planck-Gesellschaft, Berlin 14195, Germany; orcid.org/0000-0001-6371-5837

Hui Zhao – Beijing National Laboratory for Condensed Matter Physics and Institute of Physics, Chinese Academy of Sciences, Beijing 100190, P. R. China

Complete contact information is available at:

<https://pubs.acs.org/doi/10.1021/acsnano.2c03809>

Author Contributions

*Y.Q. and M.-X.G. contributed equally.

Author Contributions

Y.Q. and R.E. designed the experiments. Y.Q. executed the experiments with help from D.Z., T.V., H.S., and Y.W. Y.Q. did the data analysis and the structure factor calculations. M.G., H.Z., and S.M. did the TDDFT-MD simulation. Y.Q. wrote the manuscript with contributions from all the authors.

Notes

The authors declare no competing financial interest.

All data needed to evaluate the conclusions in the paper are present in the paper and/or the Supporting Information. Additional data related to this paper may be requested from the authors.

ACKNOWLEDGMENTS

This work was funded by the Max Planck Society and the European Research Council (ERC) under the European Union's Horizon 2020 research and innovation program (Grant Agreement No. ERC-2015-CoG-682843). Y.Q. ac-

knowledge support by the Sino-German (CSC-DAAD) Postdoc Scholarship Program (Grants No. 201709920054 and No. 57343410) and funding from the Max Plank Society.

REFERENCES

- (1) Wang, Y.; Xiao, J.; Zhu, H.; Li, Y.; Alsaied, Y.; Fong, K.; Zhou, Y.; Wang, S.; Shi, W.; Wang, Y.; Zettl, A.; Reed, E. J.; Zhang, X. Structural Phase Transition In Monolayer MoTe_2 Driven By Electrostatic Doping. *Nature* **2017**, *550*, 487.
- (2) Keum, D.; Cho, S.; Kim, J.; Choe, D.; Sung, H.; Kan, M.; Kang, H.; Hwang, J.; Kim, S.; Yang, H.; Chang, K. J.; Lee, Y. Bandgap Opening In Few-Layered Monoclinic MoTe_2 . *Nat. Phys.* **2015**, *11*, 482.
- (3) Ali, M.; Xiong, J.; Flynn, S.; Tao, J.; Gibson, Q.; Schoop, L.; Liang, T.; Haldolaarachchige, N.; Hirschberger, M.; Ong, N. P.; Cava, R. J. Large, Non-Saturating Magnetoresistance In WTe_2 . *Nature* **2014**, *514*, 205–208.
- (4) Qian, X.; Liu, J.; Fu, L.; Li, J. Quantum Spin Hall Effect In Two-Dimensional Transition Metal Dichalcogenides. *Science* **2014**, *346*, 1344.
- (5) Tang, S.; Zhang, C.; Wong, D.; Pedramrazi, Z.; Tsai, H.; Jia, C.; Moritz, B.; Claassen, M.; Ryu, H.; Kahn, S.; Jiang, J.; Yan, H.; Hashimoto, M.; Lu, D.; Moore, R. G.; Hwang, C.; Hwang, C.; Hussain, Z.; Chen, Y.; Ugeda, M. M.; Liu, Z.; Xie, X.; Devereaux, T. P.; Crommie, M. F.; Mo, S.; Shen, Z. Quantum Spin Hall State In Monolayer $1\text{T}'\text{-WTe}_2$. *Nat. Phys.* **2017**, *13*, 683.
- (6) Fei, Z.; Palomaki, T.; Wu, S.; Zhao, W.; Cai, X.; Sun, B.; Nguyen, P.; Finney, J.; Xu, X.; Cobden, D. H. Edge Conduction In Monolayer WTe_2 . *Nat. Phys.* **2017**, *13*, 677.
- (7) Wu, S.; Fatemi, V.; Gibson, Q. D.; Watanabe, K.; Taniguchi, T.; Cava, R. J.; Jarillo-Herrero, P. Observation Of The Quantum Spin Hall Effect Up To 100 K In A Monolayer Crystal. *Science* **2018**, *359*, 76.
- (8) Deng, K.; Wan, G.; Deng, P.; Zhang, K.; Ding, S.; Wang, E.; Yan, M.; Huang, H.; Zhang, H.; Xu, Z.; Denlinger, J.; Fedorov, A.; Yang, H.; Duan, W.; Yao, H.; Wu, Y.; Fan, S.; Zhang, H.; Chen, X.; Zhou, S. Experimental Observation Of Topological Fermi Arcs In Type-II Weyl Semimetal MoTe_2 . *Nat. Phys.* **2016**, *12*, 1105–1110.
- (9) Tamai, A.; Wu, Q. S.; Cucchi, I.; Bruno, F. Y.; Riccò, S.; Kim, T. K.; Hoesch, M.; Barreteau, C.; Giannini, E.; Besnard, C.; Soluyanov, A. A.; Baumberger, F. Fermi Arcs And Their Topological Character In The Candidate Type-II Weyl Semimetal MoTe_2 . *Phys. Rev. X* **2016**, *6*, 031021.
- (10) Huang, L.; McCormick, T. M.; Ochi, M.; Zhao, Z.; Suzuki, M.; Arita, R.; Wu, Y.; Mou, D.; Cao, H.; Yan, J.; Trivedi, N.; Kaminski, A. Spectroscopic Evidence For A Type II Weyl Semimetallic State In MoTe_2 . *Nat. Mater.* **2016**, *15*, 1155–1160.
- (11) Jiang, J.; Liu, Z. K.; Sun, Y.; Yang, H. F.; Rajamathi, C. R.; Qi, Y. P.; Yang, L. X.; Chen, C.; Peng, H.; Hwang, C.-C.; Sun, S. Z.; Mo, S.-K.; Vobornik, I.; Fujii, J.; Parkin, S. S. P.; Felser, C.; Yan, B. H.; Chen, Y. L. Signature Of Type-II Weyl Semimetal Phase In MoTe_2 . *Nat. Commun.* **2017**, *8*, 13973.
- (12) Soluyanov, A.; Gresch, D.; Wang, Z.; Wu, Q.; Troyer, M.; Dai, X.; Bernevig, B. Type-II Weyl Semimetals. *Nature* **2015**, *527*, 495.
- (13) Tang, F.; Po, H.; Vishwanath, A.; Wan, X. Efficient Topological Materials Discovery Using Symmetry Indicators. *Nat. Phys.* **2019**, *15*, 470.
- (14) Wang, Z.; Wieder, B.; Li, J.; Yan, B.; Bernevig, B. Higher-Order Topology, Monopole Nodal Lines, And The Origin Of Large Fermi Arcs In Transition Metal Dichalcogenides XTe_2 ($\text{X} = \text{Mo}, \text{W}$). *Phys. Rev. Lett.* **2019**, *123*, 186401.
- (15) Li, P.; Wen, Y.; He, X.; Zhang, Q.; Xia, C.; Yu, Z.; Yang, S. A.; Zhu, Z.; Alshareef, H. N.; Zhang, X. Evidence For Topological Type-II Weyl Semimetal WTe_2 . *Nat. Commun.* **2017**, *8*, 2150.
- (16) Choi, Y.; Xie, Y.; Chen, C.; Park, J.; Song, S.; Yoon, J.; Kim, B. J.; Taniguchi, T.; Watanabe, K.; Kim, J.; Fong, K.; Ali, M. N.; Law, K.; Lee, G. Evidence Of Higher-Order Topology In Multilayer WTe_2 From Josephson Coupling Through Anisotropic Hinge States. *Nat. Mater.* **2020**, *19*, 974–979.
- (17) Choe, D.; Sung, H.; Chang, K. J. Understanding Topological Phase Transition In Monolayer Transition Metal Dichalcogenides. *Phys. Rev. B* **2016**, *93*, 125109.
- (18) Senthil, T. Symmetry-Protected Topological Phases Of Quantum Matter. *Annu. Rev. Condens. Matter Phys.* **2015**, *6*, 299–324.
- (19) Tang, F.; Po, H.; Vishwanath, A.; Wan, X. Comprehensive Search For Topological Materials Using Symmetry Indicators. *Nature* **2019**, *566*, 486–489.
- (20) Vergniory, M.; Elcoro, L.; Felser, C.; Regnault, N.; Bernevig, B.; Wang, Z. A Complete Catalogue Of High-Quality Topological Materials. *Nature* **2019**, *566*, 480–485.
- (21) Zhang, T.; Jiang, Y.; Song, Z.; Huang, H.; He, Y.; Fang, Z.; Weng, H.; Fang, C. Catalogue Of Topological Electronic Materials. *Nature* **2019**, *566*, 475–479.
- (22) Sie, E. J.; Nyby, C. M.; Pemmaraju, C. D.; Park, S.; Shen, X.; Yang, J.; Hoffmann, M. C.; Ofori-Okai, B. K.; Li, R.; Reid, A. H.; Weathersby, S.; Mannebach, E.; Finney, N.; Rhodes, D.; Chenet, D.; Antony, A.; Balicas, L.; Hone, J.; Devereaux, T. P.; Heinz, T. F.; Wang, X.; Lindenberg, A. M. An Ultrafast Symmetry Switch In A Weyl Semimetal. *Nature* **2019**, *565*, 61.
- (23) Zhang, M. Y.; Wang, Z. X.; Li, Y. N.; Shi, L. Y.; Wu, D.; Lin, T.; Zhang, S. J.; Liu, Y. Q.; Liu, Q. M.; Wang, J.; Dong, T.; Wang, N. L. Light-Induced Subpicosecond Lattice Symmetry Switch In MoTe_2 . *Phys. Rev. X* **2019**, *9*, 021036.
- (24) Hein, P.; Jauernik, S.; Erk, H.; Yang, L.; Qi, Y.; Sun, Y.; Felser, C.; Bauer, M. Mode-Resolved Reciprocal Space Mapping Of Electron-Phonon Interaction In The Weyl Semimetal Candidate $1\text{T}'\text{-WTe}_2$. *Nat. Commun.* **2020**, *11*, 2613.
- (25) Tang, C. S.; Yin, X.; Wee, A. T. S. 1D Chain Structure In $1\text{T}'\text{-Phase 2D Transition Metal Dichalcogenides And Their Anisotropic Electronic Structures}$. *Appl. Phys. Rev.* **2021**, *8*, 011313.
- (26) Chatelain, R.; Morrison, V.; Klarenaar, B.; Siwick, B. J. Coherent And Incoherent Electron-Phonon Coupling In Graphite Observed With Radio-Frequency Compressed Ultrafast Electron Diffraction. *Phys. Rev. Lett.* **2014**, *113*, 235502.
- (27) Waldecker, L.; Berton, R.; Ernst, R. Compact Femto-second Electron Diffractometer With 100 KeV Electron Bunches Approaching The Single-Electron Pulse Duration Limit. *J. Appl. Phys.* **2015**, *117*, 044903.
- (28) Zhang, K.; Bao, C.; Gu, Q.; Ren, X.; Zhang, H.; Deng, K.; Wu, Y.; Li, Y.; Feng, J.; Zhou, S. Raman Signatures Of Inversion Symmetry Breaking And Structural Phase Transition In Type-II Weyl Semimetal MoTe_2 . *Nat. Commun.* **2016**, *7*, 13552.
- (29) Zeiger, H. J.; Vidal, J.; Cheng, T. K.; Ippen, E. P.; Dresselhaus, G.; Dresselhaus, M. S. Theory For Displacive Excitation Of Coherent Phonons. *Phys. Rev. B* **1992**, *45*, 768.
- (30) Li, J. J.; Chen, J.; Reis, D. A.; Fahy, S.; Merlin, R. Optical Probing Of Ultrafast Electronic Decay In Bi And Sb With Slow Phonons. *Phys. Rev. Lett.* **2013**, *110*, 047401.
- (31) Bothschafter, E. M.; Paarmann, A.; Zijlstra, E. S.; Karpowicz, N.; Garcia, M. E.; Kienberger, R.; Ernst, R. Ultrafast Evolution Of The Excited-State Potential Energy Surface Of TiO_2 Single Crystals Induced By Carrier Cooling. *Phys. Rev. Lett.* **2013**, *110*, 067402.
- (32) Frigge, T.; Hafke, B.; Witte, T.; Krenzer, B.; Streubühr, C.; Syed, A. S.; Trontl, V. M.; Avigo, I.; Zhou, P.; Ligges, M.; von der Linde, D.; Bovensiepen, U.; Horn-von Hoegen, M.; Wippermann, S.; Lücke, A.; Sanna, S.; Gerstmann, U.; Schmidt, W. G. Optically Excited Structural Transition In Atomic Wires On Surfaces At The Quantum Limit. *Nature* **2017**, *544*, 207–211.
- (33) Eichberger, M.; Schäfer, H.; Krumova, M.; Beyer, M.; Demsar, J.; Berger, H.; Moriena, G.; Sciaini, G.; Miller, R. J. D. Snapshots Of Cooperative Atomic Motions In The Optical Suppression Of Charge Density Waves. *Nature* **2010**, *468*, 799.
- (34) Ji, S.; Grånäs, O.; Weissenrieder, J. Manipulation Of Stacking Order In $1\text{T}'\text{-WTe}_2$ By Ultrafast Optical Excitation. *ACS Nano* **2021**, *15*, 8826.

- (35) Ideta, S.-i.; Zhang, D.; Dijkstra, A. G.; Artyukhin, S.; Keskin, S.; Cingolani, R.; Shimojima, T.; Ishizaka, K.; Ishii, H.; Kudo, K.; Nohara, M.; Miller, R. J. D. Ultrafast Dissolution And Creation Of Bonds In IrTe₂ Induced By Photodoping. *Sci. Adv.* **2018**, *4*, No. eaar3867.
- (36) Wall, S.; Yang, S.; Vidas, L.; Chollet, M.; Glowina, J. M.; Kozina, M.; Katayama, T.; Henighan, T.; Jiang, M.; Miller, T. A.; Reis, D. A.; Boatner, L. A.; Delaire, O.; Trigo, M. Ultrafast Disorder of Vanadium Dimers In Photoexcited VO₂. *Science* **2018**, *362*, 572.
- (37) Sokolowski-Tinten, K.; Blome, C.; Blums, J.; Cavalleri, A.; Dietrich, C.; Tarasevitch, A.; Uschmann, I.; Förster, E.; Kammler, M.; Horn-von-Hoegen, M.; von der Linde, D. Femtosecond X-ray Measurement Of Coherent Lattice Vibrations Near The Lindemann Stability Limit. *Nature* **2003**, *422*, 287–289.
- (38) Haupt, K.; Eichberger, M.; Erasmus, N.; Rohwer, A.; Demsar, J.; Rossmagel, K.; Schwoerer, H. Ultrafast Metamorphosis Of A Complex Charge-Density Wave. *Phys. Rev. Lett.* **2016**, *116*, 016402.
- (39) Mar, A.; Jobic, S.; Ibers, J. A. Metal-Metal VS Tellurium-Tellurium Bonding In WTe₂ And Its Ternary Variants TaIrTe₄ And NbIrTe₄. *J. Am. Chem. Soc.* **1992**, *114*, 8963.
- (40) Canadell, E.; LeBeuze, A.; El Khalifa, M. A.; Chevrel, R.; Whangbo, M. H. Origin Of Metal Clustering In Transition-Metal Chalcogenide Layers MX₂ (M = Nb, Ta, Mo, Re; X = S, Se). *J. Am. Chem. Soc.* **1989**, *111*, 3778.
- (41) Song, Q.; Wang, H.; Pan, X.; Xu, X.; Wang, Y.; Li, Y.; Song, F.; Wan, X.; Ye, Y.; Dai, L. Anomalous In-Plane Anisotropic Raman Response Of Monoclinic Semimetal 1T'-MoTe₂. *Sci. Rep.* **2017**, *7*, 1758.
- (42) Guan, M. X.; Wang, E.; You, P. W.; Sun, J. T.; Meng, S. Manipulating Weyl Quasiparticles By Orbital-Selective Photoexcitation In WTe₂. *Nat. Commun.* **2021**, *12*, 1885.
- (43) Cheng, M.; Zhong, S.; Rivas, N.; Dekker, T.; Petruk, A. A.; Gicala, P.; Pichugin, K.; Chen, F.; Luo, X.; Sun, Y.; Tsen, A. W.; Sciaini, G. Photoinduced Interlayer Dynamics In Td-MoTe₂: A Broadband Pump-Probe Study. *Appl. Phys. Lett.* **2022**, *120*, 123102.
- (44) Beaulieu, S.; Dong, S.; Tancogne-Dejean, N.; Dendzik, M.; Pincelli, T.; Maklar, J.; Xian, R. P.; Sentef, M. A.; Wolf, M.; Rubio, A.; Rettig, L.; Ernstorfer, R. Ultrafast Dynamical Lifshitz Transition. *Sci. Adv.* **2021**, *7*, No. eabd9275.
- (45) Qi, Y. P.; Chen, N. K.; Vasileiadis, T.; Zahn, D.; Seiler, H.; Li, X. B.; Ernstorfer, R. Photoinduced Ultrafast Transition Of The Local Correlated Structure In Chalcogenide Phase-Change Materials. *arXiv Preprint*, <https://arxiv.org/abs/2109.05705v1> (2021).
- (46) Simonov, A.; Goodwin, A. L. Designing Disorder Into Crystalline Materials. *Nat. Rev. Chem.* **2020**, *4*, 657.
- (47) Huang, Y. T.; Chen, N. K.; Li, Z. Ze.; Li, X. B.; Wang, X. P.; Chen, Q. D.; Sun, H. B.; Zhang, S. Mexican-Hat Potential Energy Surface In Two-Dimensional III₂-VI₃ Materials And The Importance Of Entropy Barrier In Ultrafast Reversible Ferroelectric Phase Change. *Appl. Phys. Rev.* **2021**, *8*, 031413.
- (48) Grigera, T. S.; Martín-Mayor, V.; Parisi, G.; Verrocchio, P. Phonon Interpretation Of The 'Boson Peak' In Supercooled Liquids. *Nature* **2003**, *422*, 289.
- (49) Martinez, P.; Blanchet, V.; Descamps, D.; Dory, J. B.; Fourment, C.; Papagiannouli, I.; Petit, S.; Raty, J. Y.; Noé, P.; Gaudin, J. Sub-Picosecond Non-Equilibrium States In The Amorphous Phase Of GeTe Phase-Change Material Thin Films. *Adv. Mater.* **2021**, *33*, 2102721.
- (50) Perez-Salinas, D.; Johnson, A. S.; Prabhakaran, D.; Wall, S. Multi-Mode Excitation Drives Disorder During The Ultrafast Melting Of A C4-Symmetry-Broken Phase. *Nat. Commun.* **2022**, *13*, 238.
- (51) Li, J.; Strand, H. U. R.; Werner, P.; Eckstein, M. Theory Of Photoinduced Ultrafast Switching To A Spin-Orbital Ordered Hidden Phase. *Nat. Commun.* **2018**, *9*, 4581.
- (52) Windsor, Y. W.; Zahn, D.; Kamrla, R.; Feldl, J.; Seiler, H.; Chiang, C.-T.; Ramsteiner, M.; Widdra, W.; Ernstorfer, R.; Rettig, L. Exchange-Striction Driven Ultrafast Nonthermal Lattice Dynamics In NiO. *Phys. Rev. Lett.* **2021**, *126*, 147202.
- (53) Qi, Y.; Naumov, P. G.; Ali, M. N.; Rajamathi, C. R.; Schnelle, W.; Barkalov, O.; Hanfland, M.; Wu, S.; Shekhar, C.; Sun, Y.; Süß, V.; Schmidt, M.; Schwarz, U.; Pippel, E.; Werner, P.; Hillebrand, R.; Förster, T.; Kampert, E.; Parkin, S.; Cava, R. J.; Felser, C.; Yan, B.; Medvedev, S. A. Superconductivity In Weyl Semimetal Candidate MoTe₂. *Nat. Commun.* **2016**, *7*, 11038.
- (54) Meng, S.; Kaxiras, E. Real-Time Local Basis-Set Implementation Of Time-Dependent Density Functional Theory For Excited State Dynamics Simulations. *J. Chem. Phys.* **2008**, *129*, 054110.
- (55) Ma, W.; Zhang, J.; Yan, L.; Jiao, Y.; Gao, Y.; Meng, S. Recent Progresses In Real-Time Local-Basis Implementation Of Time Dependent Density Functional Theory For Electron–Nucleus Dynamics. *Comput. Mater. Sci.* **2016**, *112*, 478.
- (56) Lian, C.; Guan, M.; Hu, S.; Zhang, J.; Meng, S. Photoexcitation In Solids: First-Principles Quantum Simulations By Real-Time TDDFT. *Adv. Theory. Simul.* **2018**, *1*, 1800055.
- (57) Perdew, J. P.; Burke, K.; Ernzerhof, M. Generalized Gradient Approximation Made Simple. *Phys. Rev. Lett.* **1996**, *77*, 3865.
- (58) Alonso, J. L.; Andrade, X.; Echenique, P.; Falceto, F.; Prada-Gracia, D.; Rubio, A. Efficient Formalism For Large-Scale Ab Initio Molecular Dynamics Based On Time-Dependent Density Functional Theory. *Phys. Rev. Lett.* **2008**, *101*, 096403.

Recommended by ACS

Disentangling Structural and Electronic Properties in V₂O₃ Thin Films: A Genuine Nonsymmetry Breaking Mott Transition

Federico Mazzola, Ivana Vobornik, et al.

JULY 05, 2022
NANO LETTERS

READ 

Conversion between Metavalent and Covalent Bond in Metastable Superlattices Composed of 2D and 3D Sublayers

Dasol Kim, Mann-Ho Cho, et al.

DECEMBER 05, 2022
ACS NANO

READ 

Epitaxial Growth of Single-Layer Kagome Nanoflakes with Topological Band Inversion

Sisheng Duan, Wei Chen, et al.

NOVEMBER 16, 2022
ACS NANO

READ 

Extracting the Strain Matrix and Twist Angle from the Moiré Superlattice in van der Waals Heterostructures

Dorri Halbertal, D. N. Basov, et al.

JANUARY 04, 2022
ACS NANO

READ 

Get More Suggestions >